Fuel 134 (2014) 53–62

Contents lists available at ScienceDirect

Fuel

journal homepage: www.elsevier.com/locate/fuel

Char burning kinetics from imaging pyrometry: Particle shape effects

Martin Schiemann *, Sven Haarmann, Nikita Vorobiev

Ruhr-Universität Bochum, Universitätsstraße 150, 44801 Bochum, Germany

HIGHLIGHTS

- The effect of particle shapes on pulverized fuel particles was analyzed.
- Theoretical considerations were tested and applied on experimental data.
- The particle shape was found to have an effect on the burning rate of fuel particles.
- Current models should be adapted for non-spherical particles.

ARTICLE INFO

Article history:
Received 13 March 2014
Received in revised form 20 May 2014
Accepted 20 May 2014
Available online 2 June 2014

Keywords:
Char combustion
Biomass
Burning rate
Pyrometry

ABSTRACT

Biomass combustion becomes increasingly important in nowadays energy production. One of the major differences between biomass and coal is the particle shape. Therefore the effect of particle shape variations was calculated to determine the effect of spheroidal or cylindrical particle shapes when determining char burning kinetics of pulverized fuel particles from pyrometric measurements. A model frequently used for char kinetics determination was adapted to spheroidal and cylindrical particles under typical combustion conditions. The impact of the particle shape on the energy balance, which is needed for the determination of kinetics parameters, was calculated for typical particle sizes and length to diameter ratios. As the calculations show, the influence of particle shape effects is not negligible for the determination of biomass char burning parameters by pyrometric measurements. The application of the adapted model on measured data shows, that particle shape effects can be resolved by pyrometric techniques. The results presented indicate that a sound analysis of the particle burning rate should include a three-dimensional particle shape measurement.

© 2014 Elsevier Ltd. All rights reserved.

1. Introduction

Due to the demand for carbon-neutral fuels, the amount of biomass replacing coal in pulverized fuel boilers is increasing [1]. In pulverized fuel (pf) combustion, the combustion of char (fixed carbon) is the time-determining step. Design of pf-boilers, which is usually supported by CFD-simulations, requires an exact prediction of the char burning rate, both for the determination of spatial heat release and for sufficient burn out.

At least three competing techniques to determine char burning kinetics are known in literature. TGA experiments have been performed on a variety of fuels (coals, raw and torrefied biomass) under air-fired and oxy-fuel conditions [2–4]. In TGA experiments, the temperature is usually kept low enough to assure chemically controlled (Zone-I) combustion conditions, but at low heating rates which are not typical for pf-combustion. Typical heating rates are easily achieved in drop tube reactors (DTR) or entrained flow reactors (EFR), which have been applied to study the combustion and gasification rates of coal and biomass char under air-fired and oxy-fuel conditions [2,5]. In DTRs the fuel particles follow a linear trajectory at a nearly constant velocity, which simplifies the determination of residence times. A common technique to determine the reaction kinetics parameters is sampling of solid combustion residues. These samples are then used to measure the degree of conversion by the so-called ash tracer method [6].

1.1. Optical determination of burning rates: state of the art

Another method to determine the apparent reaction kinetics of char particles in DTRs is two-color pyrometry. This method is based on measuring temperature and diameter of a single burning char particle under well-defined conditions. From these experimental data, the energy balance around the particle is calculated.

Several research groups have deployed ratio pyrometers in two or three-color versions to determine char burning rates. At Sandia

---

* Corresponding author. Tel.: +49 234 32 27362.
E-mail address: schiemann@leat.rub.de (M. Schiemann).

http://dx.doi.org/10.1016/j.fuel.2014.05.049
0016-2361/© 2014 Elsevier Ltd. All rights reserved.

Nomenclature

A_o	pre-exponential factor (mol/(m^2 s))
A	area (m^2)
A_{cyl}	cylinder surface (m^2)
A_s	outer surface area (m^2)
c_p	heat capacity of char (J/(kg K))
d	minor particles' axis (ellipsoid), diameter (cylinder)
d_A	surface diameter (μm)
d_{char}	characteristic diameter (μm)
d_p	particle diameter (μm)
d_{sphere}	diameter of particle with equal projection area (μm)
d_V	volume diameter (μm)
E_a	activation energy (J/mol)
h	heat transfer coefficient (W/(m^2 K))
ΔH	heat of reaction (J/mol)
L	largest dimension of particle (m)
n	reaction order (–)
n_{px}	number of pixels
Nu	Nusselt number (–)
$p_{O_2,s}$	O_2-pressure at a particles' surface (Pa)
q	burning rate (mol/(m^2 s))
q_{cyl}	burning rate assuming cylindrical particle (mol/(m^2 s))
q_{ell}	burning rate assuming elliptical particle (mol/(m^2 s))
q_{sphere}	burning rate assuming spherical particles (mol/(m^2 s))
$\dot{q}_{conv}$	convective heat flux R (W/m^2)
$\dot{q}_{inert}$	heat flux into the non-reacting particle (W/m^2)
$\dot{q}_i$	heat flux (W/m^2)
$\dot{q}_{rad}$	radiative heat flux (W/m^2)
$\dot{q}_{react}$	surface-specific heat of reaction (W/m^2)
Q_i	energy of type i (J)
R	molar gas constant (J/(mol K))
s_{px}	pixel size (μm)
t	time (s)
T_f	film temperature (K)
T_g	gas temperature (K)
T_p	particle temperature (K)
T_w	wall temperature (K)
v_p	particle velocity (m/s)
V_{cyl}	cylinder volume (m^3)
V_p	particle volume (m^3)
x	variable (–)
z	distance to fuel inlet (EFR) (m)
α	heat transfer coefficient (W/(m^2 K))
ε	emissivity (–)
λ	thermal conductivity (W/(m K))
ρ_p	char density (kg/m^3)
σ	Stefan–Boltzmann constant ($5.67 * 10^{-8}$ (W/(m^2 K^4)))

National Laboratories, two-color pyrometry of burning char particles in an EFR has been carried out for a long period. From the late 1970s on, coal and biomass chars have been investigated for their burning behaviour [7–13]. This system is based on a coded aperture for particle size detection. As the particle size is deduced from intensities measured by photo multipliers (PMT), the particle shape is assumed to be spherical. Another system based on size measurement by a coded aperture has been developed by Cope et al. [14], also using PMTs to measure the intensity of burning coal char particles. Other groups developed systems using fibre optics to guide particle radiation to PMTs, e.g. Spliethoff et al. [15] and Joutsenoja et al. [16,17], both using pyrometric data from single burning particles to determine char burning rates. All pyrometers mentioned so far have in common to measure in radial direction perpendicular to the coal streak in an EFR or DTR. Therefore only a momentary of each particle passing the pyrometers field of view is detected. Typically, a number of particles sufficient for reliable statistics are collected at a specified distance to the solid fuel inlet, and several measurements at different distances (residence times) are required to cover the burning history of a fuel sample. Another approach has been chosen in the work of Levendis and his group. The pyrometer system, described in detail in [18], measures along the axis of the EFR, which allows to measure the complete trajectory of a single particle. Thus, beneath the determination of particle temperatures [19], the burning time can be measured directly [20,21]. Particle burning rates have been derived from these measurements [20], and literature data has been tested to fit the measured burning times and particle temperatures of different coal samples with good agreement [21].

A system based on intensified (I)CCD cameras has been used to measure particle temperature and size by two-color pyrometry by Hackert et al. [22]. As the ICCD imaging technique provides spatially resolved 2d-images of burning particles with a resolution of 10 μm or less, particles of typical size for pf-firing (d_p = 50–100 μm) can be resolved spatially. The pyrometer system has been used for further investigation of coal and biomass chars, an example on particle temperature measurement of coal chars in oxyfuel atmospheres is given in [23].

While coal particles in pf-applications are typically compact and nearly spherical, even for those particles shape effects have been considered in literature [24]. Biomass particles originating from woody and herbaceous fuels show severe deviations from the spherical shape [25–27]. As will be described in the following, the particle shape has to be considered when deriving char burning kinetics from pyrometric measurements, as the energy balance, which is the key element of burning rate calculations, is affected by the particle shape. As the fibrous structure of biomass particles leads to particle shapes which can be assumed to be cylindrical or ellipsoidal, both shapes are tested in theory and on exemplary measurements.

2. Char burning kinetics from pyrometry

2.1. Energy balance around burning particles

The key element of burning rate determination by pyrometry is the energy flow balance at the outer surface of a particle:

$$\dot{q}_{react} = \dot{q}_{rad} + \dot{q}_{conv} + \dot{q}_{inert}\left[\frac{J}{m^2 s}\right]. \tag{1}$$

As shown in Eq. (1), the energy produced by reaction is balanced by the radiative heat transfer between the particle and its surrounding, the convective heat transfer between particle and gas phase and the temperature change of the inert particle (the non-reacting char and ash). In the following, the participating energy fluxes are calculated for particles of spherical, prolate ellipsoidal and cylindrical shape (Fig. 1).

In general it is assumed, that the surface temperature is constant and the heat and mass transfer are homogeneous, so that the surface dependency of $\dot{q}_i = dQ_i/(dt * dA)$ can be expressed by setting $dA = A_s$, where A_s denotes the particles outer surface. Under the given assumptions, the expressions for the reaction energy and the radiative heat transfer are shape-independent, as shown in Table 1. The reaction part of the heat flux is calculated from the surface reaction rate q and the heat of reaction ΔH:

$$\dot{q}_{react} = q\Delta H. \tag{2}$$

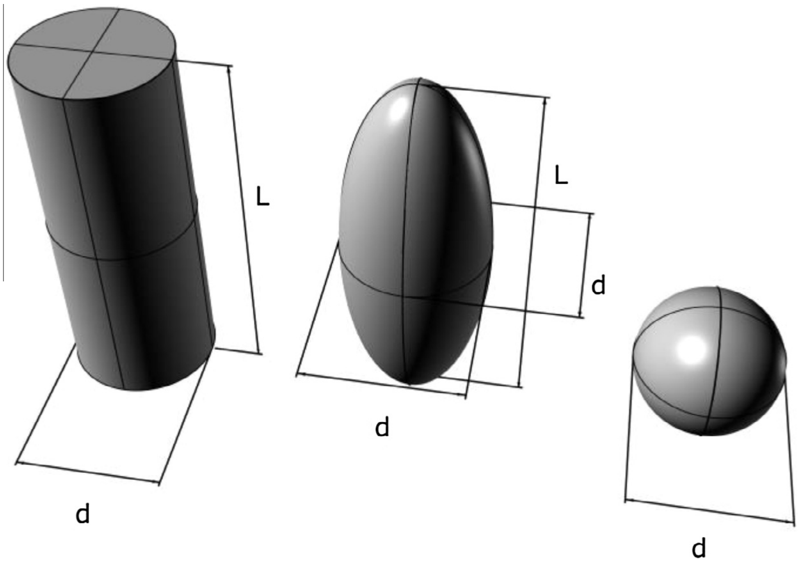

Fig. 1. Shapes of the model particles considered, $L/d = 2.5$.

Table 1
Volume/surface ratio for spherical, prolate ellipsoidal and cylindrical particles.

	Sphere	Prolate ellipsoid	Cylinder
V_p/A_s (m)	$\frac{d}{6}$	$\frac{Ld}{12\left(d+\frac{L^2}{\sqrt{L^2-d^2}}\arcsin\frac{\sqrt{L^2-d^2}}{L}\right)}$	$\frac{Ld}{2(d+2L)}$

The radiative heat transfer is calculated from the Stefan–Boltzmann constant σ, the particles emissivity ε, its temperature und the wall temperature (possible effects of gas species affecting the radiative heat flux are usually neglected):

$$\dot{q}_{rad} = \sigma\varepsilon\left(T_p^4 - T_w^4\right). \tag{3}$$

To calculate the convective heat transfer ($\dot{q}_{conv} = h(T_p - T_g)$) between the particle and the gas phase, the heat transfer coefficient h can be calculated as:

$$h = \frac{Nu\lambda}{d_{char}}, \tag{4}$$

where Nu is the Nusselt number, λ is the average thermal conductivity of the boundary layer, and d_{char} is the characteristic diameter of the particle. For pf-particles in EFR reactors the assumption of $Nu = 2$ is valid as the relative velocity between particle and gas phase is usually negligible [9].

The calculation of the energy balance presented above is based on the single-film model, meaning that direct oxidation of the particle surface occurs, where CO and/or CO_2 are produced. The CO is oxidized in the free stream, not affecting the particles heat balance [28]. This assumption is acceptable for particles in the size range of 50–100 μm.

The effect of Stefan flow produced by the simultaneous production of CO and CO_2 is known to influence the char burning rate by several percent depending on the conditions applied [29,30]. For particle temperatures below 2000 K it seems acceptable to neglect this effect leading to only slightly underdetermined burning rates, as the results in [29] show.

2.2. Energy balance for non-spherical particles

Two summands in Eq. (1) depend on the particle shape, $\dot{q}_{inert}$ and $\dot{q}_{conv}$. The heat flux into the non-reacting particle (remaining carbon and ash) is shape-dependent, as the particle is assumed to be of constant density resulting in the necessity to calculate the ratio V_p/A_s. To calculate $\dot{q}_{inert} = (V_p/A_s)\rho_p c_p v_p dT_p/dz$, the density of the char ρ_p, its heat capacity c_p, the absolute particle velocity v_p and the temperature change depending on the distance to the fuel inlet dT_p/dz are taken into account. The last two parameters are typical for optical EFR-experiments, were the absolute particle velocity can be measured easily and the temperature change is calculated from the change in the average temperature along the particles trajectory. The resulting volume/surface ratios $\frac{V_p}{A_s}$ are given in Table 1, where L and d denote the diameter and height (cylinder) respective long and short axes (Fig. 1).

Shape coefficients are necessary to calculate the heat transfer coefficient for particles of arbitrary shape. Furthermore, d_{char} has to be chosen properly to match the shape of the particle, as shown by Wadewitz and Specht [31]. The sieve diameter, which is usually applied to characterize the particle size of pulverized fuel, is not sufficient without correction. As an alternative, the surface diameter d_A and the volume diameter d_V were found as best alternatives when calculating the heat transfer by convection using:

$$Nu = \frac{\alpha A}{\lambda}\frac{d_{char}}{A}. \tag{5}$$

The factor $(\alpha A)/\lambda$ is called shape coefficient. For the three particle shapes considered here, the resulting shape coefficients are listed in Table 2. These are chosen for particles following the surrounding gas stream slip-free, which is a typical assumption in EFR-experiments.

Based on the formulae for shape coefficients and the Nu-Correlation given in Table 2 and Eq. (5), the convective heat flux:

$$\dot{q}_{conv} = \frac{Nu\lambda}{d_{char}}(T_p - T_g) \tag{6}$$

is calculated to close the heat flux balance around burning particles. In the following, the heat balance is calculated exemplary to show

Table 2
Shape coefficients for quiescent particles.

Shape	Shape coefficient $(\alpha A)/\lambda$ (m)	Refs.
Sphere	$2\pi d$	[35,36]
Prolate ellipsoid ($L > d$)	$\frac{2\pi d\sqrt{(L/d)^2-1}}{\ln\left(L/d+\sqrt{(L/d)^2-1}\right)}$	[35,36]
Cylinder ($L > d$)	$\left[8 + 6.95(L/d)^{0.76}\right]\frac{d}{2}$	[36]

the influence of the particle shape on burning rates when the determination of burning rates is carried out by pyrometric particle temperature and diameter measurements. A number of assumptions are necessary to insert all parameters which are needed for the calculation. Typical values were chosen from [11,17,20,23]. $\dot{q}_{inert}$ was calculated using $\rho_p = 700\ \mathrm{kg/m^3}$, $c_p = 2000\ \mathrm{J/(kg\ K)}$ (both justified in [11]), $v_p = 3\ \mathrm{m/s}$ and $dT_p/dz = 2500\ \mathrm{K/m}$, both taken close to the upper limit in EFR-experiments [11,23] to show the maximum impact of these factors. From the same literature, the temperatures were chosen as $T_p = 1800\ \mathrm{K}$, $T_g = 1600\ \mathrm{K}$ and $T_w = 500\ \mathrm{K}$, the latter being typical for experiments in EFRs with quartz glass walls. The char emissivity was set to $\varepsilon = 0.8$ [9,11]. The thermal conductivity of the gas phase was set to $\lambda = 0.115\ \mathrm{W/(m\ K)}$, which is also typical for EFR experiments. The selection of variations in particle size respective the ratio *L/d* is based on the typical properties of particle size measurements in pyrometry.

2.3. Theoretical analysis of shape effects

Three cases were investigated, starting with the assumption that particles with projected surfaces of $1.96 * 10^{-9}\ \mathrm{m^2}$ ($d_{sphere} = 50\ \mu\mathrm{m}$), $7.85 * 10^{-9}\ \mathrm{m^2}$ ($d_{sphere} = 100\ \mu\mathrm{m}$) and $3.14 * 10^{-8}\ \mathrm{m^2}$ ($d_{sphere} = 200\ \mu\mathrm{m}$) were measured. The ratio *L/d* was varied from 1 (1.05 for ellipsoids, as the equations for elliptical particles are not defined for *L/d* = 1) to 10 to compare the influence of the particle shape. To study the influence of $\dot{q}_{react} = \dot{q}_{rad} + \dot{q}_{cond} + \dot{q}_{inert}$ for assumed aspherical/spherical particles, which is balanced by the heat loss mechanisms discussed, the ratio $\dot{q}_{react,aspherical}/\dot{q}_{react,sphere}$ was plotted against *L/d* in Fig. 2. Furthermore for non-spherical particles it was assumed that the orientation of the particles axis is perpendicular to the direction of view.

In the diagrams, the influences of the particle size and particle shape are clearly visible. In the case of $d_{sphere} = 50\ \mu\mathrm{m}$, the heat flux balance of the ellipsoid is equal to the sphere (lower limit) and shows a monotonic increase. At *L/d* = 10, an increase of 17% relative to the sphere with equal projection area is found, leading to a lower reaction rate assuming a spherical particle. For the cylindrical particle $\dot{q}_{react}$ is 7% smaller at *L/d* = 1 and 12% larger at *L/d* = 10, resulting in a smaller but still considerable influence on the reaction rate. With increasing particle diameter, the trend slightly changes when varying the *L/d* ratio. The ellipsoid shows little deviations from the sphere for *L/d* < 8 when $d_{sphere} = 100\ \mu\mathrm{m}$ is considered, but the cylinder shows a clearly lower $\dot{q}_{react}$ for small *L/d* ratios, which is equivalent to lower burning rates. A further increase in particle size to $d_{sphere} = 200\ \mu\mathrm{m}$ leads to permanently lower $\dot{q}_{react}$s when the particle shape is considered. For cylindrical particles, the effect reaches its maximum at *L/d* = 10, where $\dot{q}_{react}$ would be overestimated (note, that over- and underestimation is always referred to the spherical particle for comparison) by 14% assuming a sphere instead of a cylinder. For large *L/d* values, $\dot{q}_{react}$ of the prolate ellipsoid converges against the same value as the cylinder.

The results in Fig. 2 clearly indicate the importance to consider the particle shape when calculating $\dot{q}_{react}$ for burning rate determinations. As the results show, $\dot{q}_{react}$ for small particles is underestimated for a cylindrical particle (*L/d* = 1) compared to a spherical one, while the elliptical particle shape shows a steady $\dot{q}_{react}$ at this point. It must be remembered that the calculation is based on the assumption of measuring the particle size/surface for a particle with its major axis orientated orthogonally to the direction of view. The particle dimensions are included in both the heating of the inertia as V_p/A_s (Table 1) and $Nu/d = [\alpha A \lambda^{-1}]/A$, where the shape coefficient written in square brackets is taken from Table 2, which also depends on *L* and *d*. With *L/d* = *x* it follows:

$$\frac{V_{cyl}}{A_{cyl}} = \frac{d}{4}\frac{x}{x+\frac{1}{2}}. \tag{7}$$

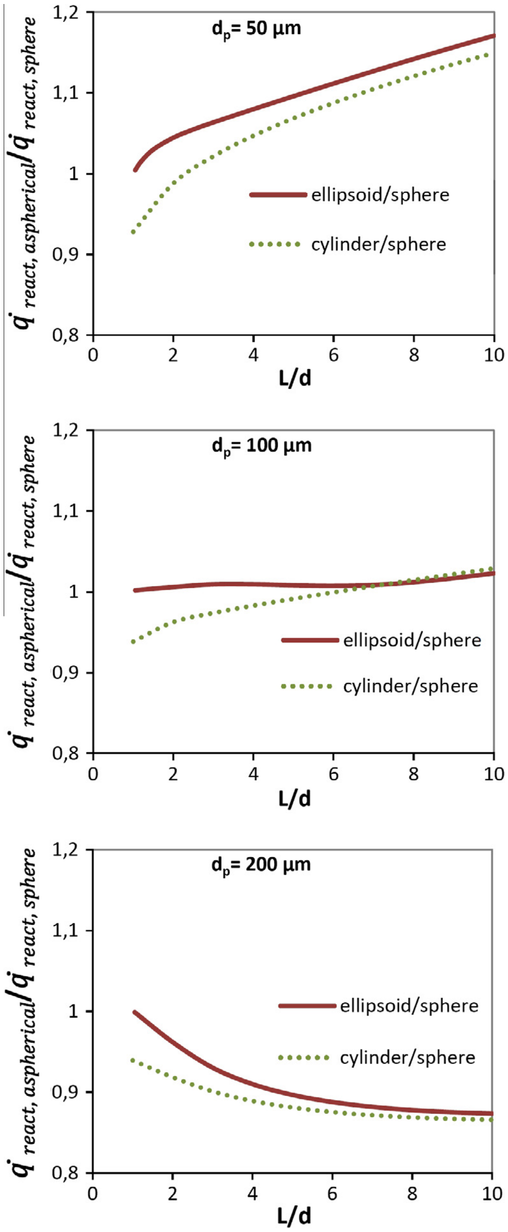

Fig. 2. $\dot{q}_{react,aspherical}/\dot{q}_{react,sphere}$ for three different particle sizes, constant projection surface area.

For spherical particles Eq. (7) becomes $d_{sphere}/6$. When the rectangular face of a cylindrical particle with *L/d* = 1 is considered, it follows that $d = d_{sphere}(\pi/4)^{1/2}$. Substituting this in Eq. (7) leads to V_{cyl}/A_{cyl} being smaller than $d_{sphere}/6$. Additionally substituting *L* by $d{\cdot}x$ leads to:

$$\frac{\alpha A}{\lambda}\frac{1}{A} = \frac{1.59}{d}. \tag{8}$$

Compared to a spherical particle, where $[\alpha A \lambda^{-1}]/A = 2/d$ is used, this reduces the convective heat flux for a given particle when *x* = 1 is applied. As is shown in Eqs. (7) and (8), for particles with small *L/d* the shape-dependent contributions differ significantly from those calculated for spherical particles, when cylindrical particles are assumed.

The contributions of heating the inertia, $\dot{q}_{inert}$, and the convective heat flux, $\dot{q}_{conv}$,the two summands expressing the shape dependency, are compared in Fig. 3 (the radiative heat flux is constant at the particle surface for given T_p and T_W). The influence

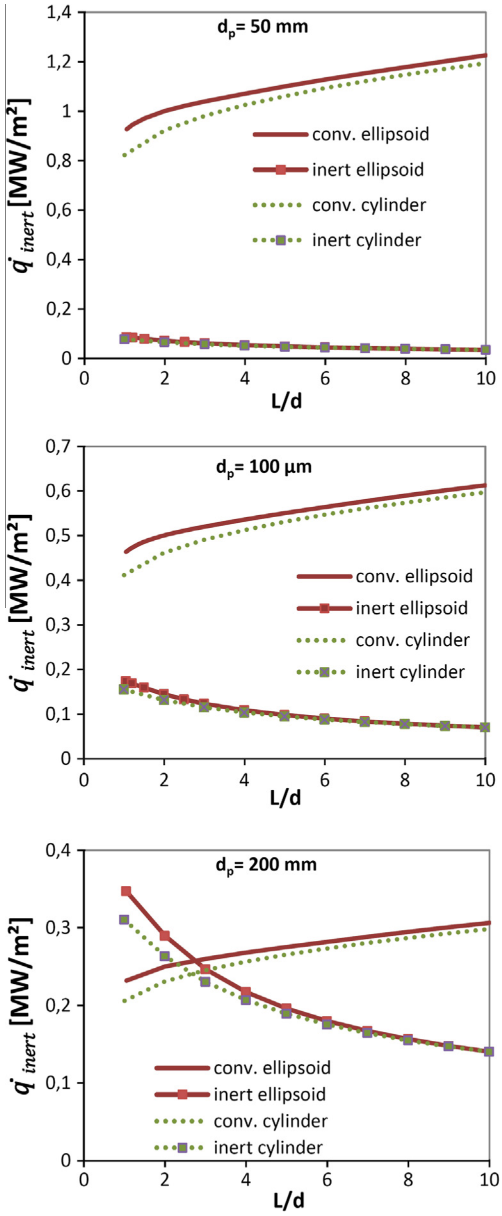

Fig. 3. $\dot{q}_{inert}$ and $\dot{q}_{cond}$ for particle sizes of 50, 100 and 200 μm.

of convective heat flux is largest for $d_{sphere} = 50$ μm, where it is four times larger than for 200 μm particles. For all particle sizes, its increase is 50% compared to the initial value of $L/d = 1$. The ratio between convective heat flux and the heat flux into the inert particle varies from 11 (cylinder, $L/d = 1$) to 35 (ellipsoid, $L/d = 10$). For the larger particles, this ratio becomes 0.72 (ellipsoid, $L/d = 1$). As Fig. 3 shows, $\dot{q}_{react}$ is influenced differently by both $\dot{q}_{inert}$ and $\dot{q}_{conv}$ for the particle shapes considered. As was mentioned before, for lower L/d ratios the difference between cylindrical and spherical (thus, elliptical particles with $L/d = 1$) becomes clearly visible here.

3. Influence on experimental results

3.1. Experimental setup and fuel

Based on the theoretical considerations presented above, the model for both particle shapes has been tested on experimental results. A flat flame burner (a laminar flow reactor with quartz glass walls for optical access, see [23], Fig. 4) was used to investigate the combustion behaviour of torrefied beech wood particles. The burner, used to provide a hot oxidizing atmosphere to expose the fuel particles to high heating rates, was fed with methane and air to achieve an atmosphere containing 7% O_2, 13% H_2O and 7% CO_2 (N_2 for balance, volumetric concentration). The gas temperature along the reactor centre line was measured with a type-S thermo couple (corrections for radiation and gas composition were applied [32]).

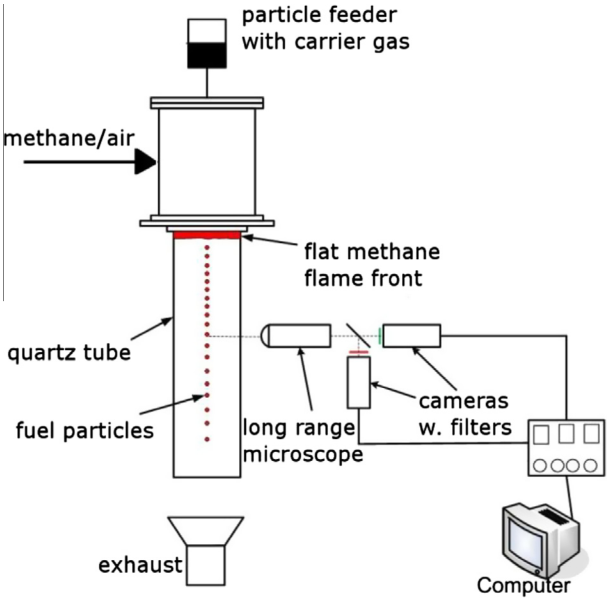

Fig. 4. Drawing of the flat flame burner and the camera system.

In this environment torrefied beech wood particles were injected, which were ground and sieved to remove particles of more than 200 μm diameter based on the mesh size. The proximate, ultimate and calorific analyses are presented in Table 3.

Furthermore the shape of the particles was analysed before the combustion experiments by a Retsch Camsizer XT. This system uses one camera to determine the two-dimensional projection of the particle shape in the viewing direction, which potentially underestimates the L/d ratio for all particles which are inclined to the direction of view. Nevertheless, the fuel particles investigated show L/d ratios much larger than unity. The particle volume fraction is plotted against L/d in Fig. 5. For 30% of the sample volume L/d ranges between 1 and 2 while 50% are in the L/d range of 2–5, and higher values complete the distribution. The data set used includes more than 900,000 particles for reliable statistics.

The particle temperature and size/shape measurement was carried out with the imaging pyrometer system TOSCA, described

Table 3
Fuel analysis.

		Torrefied beech
Prox. analysis		
Volatile matter	(wt%, dry)	71.03
Fix-carbon		28.25
Ash content		0.73
Ult. analysis		
Carbon	(wt%, dry)	56.85
Hydrogen		5.51
Nitrogen		0.32
Sulphur		0.03
Oxygen		36.96
Calorific value		
HHV	(MJ/kg, dry)	21.187

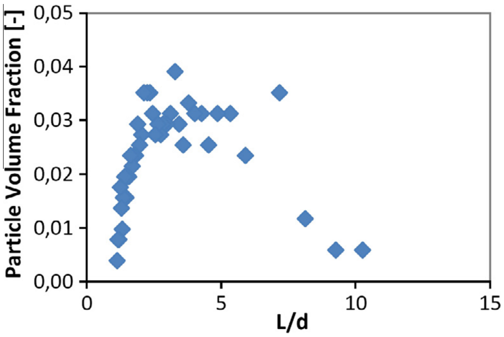

Fig. 5. Particle volume fraction of the initial beech wood sample.

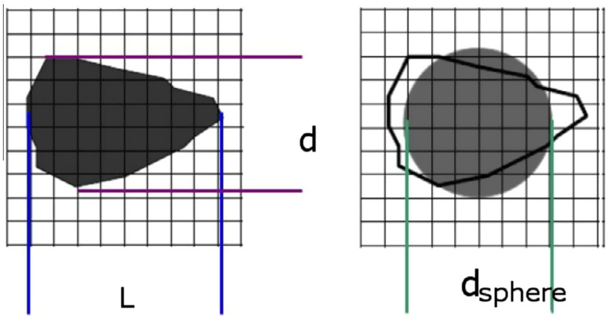

Fig. 6. Example of size detection in imaging pyrometry (left) and the standard procedure, the dark area marks the particle cross section in the line of sight respective it is outline (right).

in [23]. The camera system is temperature-calibrated from 1300–2300 K, and the spatial resolution used to measure the torrefied beech wood particles was 10.3 µm/px. In addition to the determination of particle temperature, size and shape, double exposed images were used to measure the particle velocity.

Fig. 6 shows the cross section of a virtual char particle in the line of sight of the two-dimensional, imaging pyrometer used here. The diameter d_{sphere} is calculated assuming a spherical particle shape

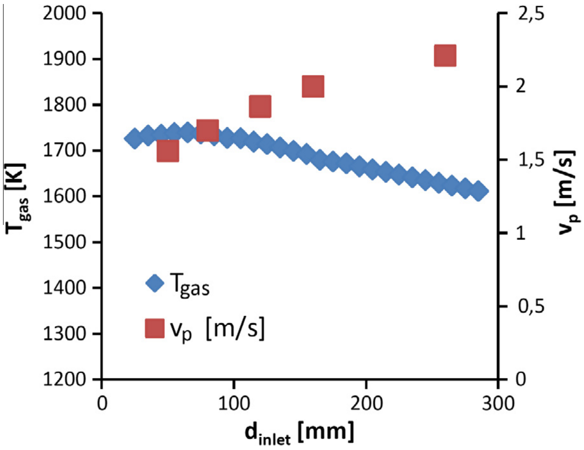

Fig. 7. Gas temperature and particle velocity.

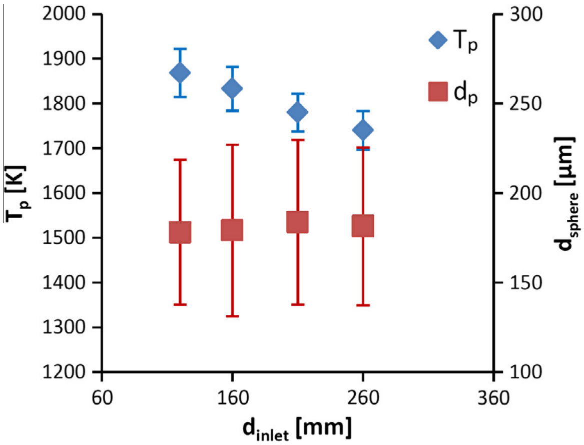

Fig. 8. Particle temperature and diameter.

with a projected surface equal to that of the non-spherical particle by counting the illuminated pixels n_{px} and calculating $d_{sphere} = 2s_{px}\sqrt{n_{px}/\pi} \cdot s_{px}$ is the size calibration factor of the camera

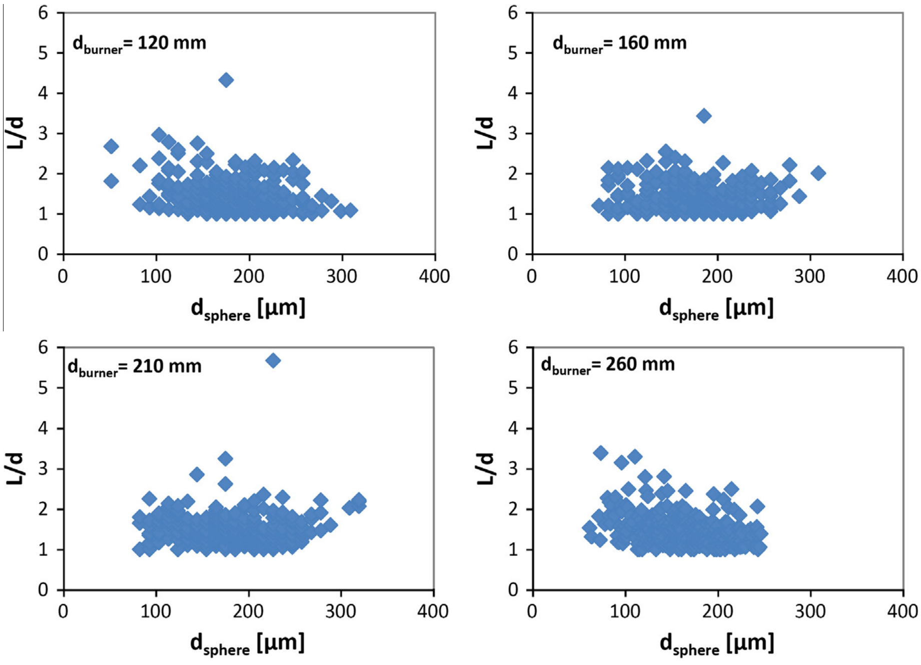

Fig. 9. Scatter plots of measured spherical diameters and L/d ratios.

system, measured with a backlight-illuminated etched grid. As is also shown in Fig. 6, the imaging pyrometer used here can resolve the particle shape directly by calculating d and L from size-calibrated images by counting the illuminated pixels in each direction. This was carried out for the data presented in the following.

3.2. Experimental results

The gas temperature profile is depicted in Fig. 7 together with the mean particle velocity against the distance from the particle inlet. The gas temperature at the reactor centre line shows a slight increase directly downstream the particle inlet, followed by an almost linear decrease. In the relevant region (120–260 mm from the particle inlet), the gas temperature decreases from 1730 to 1620 K. The mean particle velocity is given in Fig. 7 and was used to calculate the burning rate equations in the following.

The particle temperatures and diameters (averages from more than 300 particles at each point) are presented in Fig. 8. The temperatures plotted against the distance to the fuel inlet show a clear trend from an initial temperature of 1870 K down to 1740 K. The standard deviation of the temperature measurement is less than 65 K for each measurement. The particle sizes, also depicted in Fig. 8, are 175 μm (d_{sphere}) in average, with a standard deviation of approx 75 μm.

As Fig. 8 already shows, the data sets show a certain spread in the measured particle dimensions. Further insight into the dependence of the measured L/d ratio in relation to the spherical diameter determined is given by Fig. 9. The majority of the particles show L/d ratios between 1 and 2, only few particles exceed an L/d ratio above 3. Compared to the initial sample presented in Fig. 5, the fraction of high L/d ratios is reduced. This is in agreement with literature describing the influence of fast pyrolysis [33], which the particles have experienced in the experiment presented. In general, smaller particles tend to larger L/d values, a fact which will be of importance later on.

3.3. Burning rate analysis

For each particle included in the data sets for Fig. 8 the burning rate q was calculated based on Eq. (1) and Tables 1 and 2, dividing the right hand side of Eq. (1) by ΔH. The thermal conductivity was calculated for the film temperature $T_f = (T_p - T_{gas})/2$ assuming free stream gas composition as described in [34]. The heat of reaction ΔH was calculated assuming that CO is the only reaction product.

Fig. 10 illustrates the particle burning rates for more than 300 particles which represent the data set collected 260 mm downstream of the particle inlet. As the three diagrams show, the difference of the three particle shapes is not visible on first sight. This was already predicted in Section 2.3. The still small but clearest differences can be recognized for burning rates around 10 and 1 mol/(m^2 s). For q = 10 mol/(m^2 s) the burning rates assuming elliptical particles appear to be a few percent higher than those calculated for spherical particles, while those of cylindrical particles appear to be slightly lower. At the lower limit the burning rates of cylindrical particles appear to be higher than those of elliptical and spherical particles. However, a detailed quantitative analysis of the effect of particle shape assumptions for burning rate determination seems to be difficult based on these plots.

To get a better impression of the effect of different L/d ratio on the burning rate under the assumption of different particle shapes, average burning rates were calculated for L/d ratios in intervals smaller 1.1 and from 1.1 to 2.1 in steps of 0.2, as is shown in Fig. 11. All particles with L/d ratios above 2.1 were summarized in one data point. For each L/d ratio, the averaged burning rate q_{sphere}/q_{cyl} respective q_{sphere}/q_{ell} was calculated to point out the difference between the two models. Error bars indicating one standard deviation of the average burning rate ratio show the scattering of the data. The results calculated from all four data sets show roughly comparable results. The comparison between the average burning rates using models for spherical and cylindrical particles show only little deviations from unity. The burning rate calculated for spherical particles is only a few percent higher than that calculated for cylindrical particles. However, for the data set recorded at the maximum distance from the fuel inlet (z = 260 mm), where the lowest average particle temperature is found (Fig. 8), q_{sphere}/q_{cyl} is clearly larger than 1, showing higher burning rates calculated for spherical particles. The ratio q_{sphere}/q_{ell} shows a clear tendency to higher burning rates determined for elliptical particles at each point included in the analysis, especially for larger L/d intervals.

The results presented in Fig. 11 demonstrate the influence of different particle shape assumptions on the burning rates determined from (2d-) pyrometric burning rate analysis. In Fig. 12, the L/d ratio and the burning rate ratios are grouped for d_{sphere}-intervals to investigate the influence of the particle size on the burning rate determined for the different models. The vertical error bars indicate the standard deviation of each average value, while the horizontal bars represent one standard deviation of d_{sphere}, which only acts as an indicator for the size interval presented (the whole

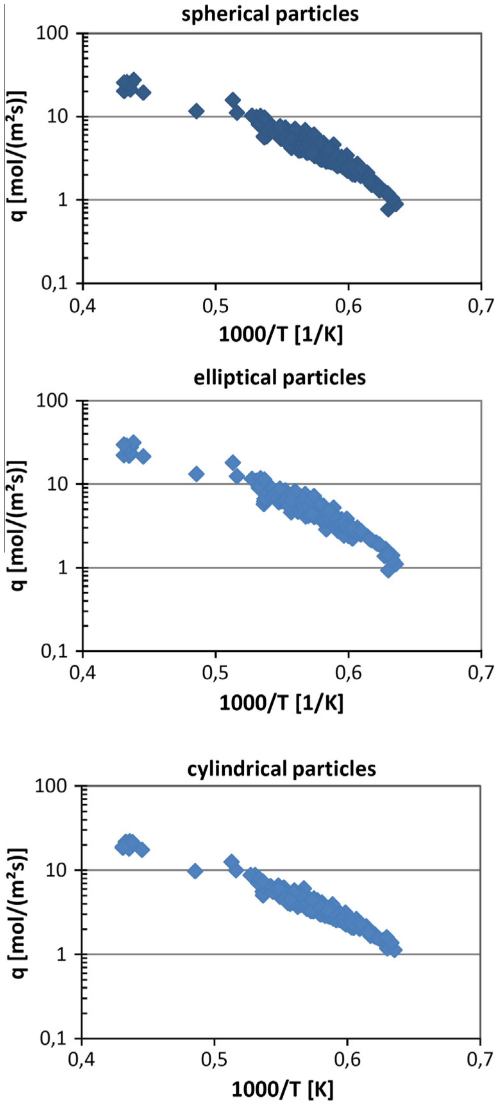

Fig. 10. Burning rates of particles from one measured data set under assumption of three different particle shapes, distance to fuel inlet 260 mm.

particle size distribution (*psd*) is nearly Gaussian, whereas the separated intervals cannot be Gaussian as splitted parts of the whole *psd*). The average *L/d* ratio ranges from 1.8 to 1.4, baring a slight tendency to decreasing values with increasing d_{sphere}. In contrast to the results presented in Fig. 11, the size-dependent burning rate ratios show clear tendencies. For q_{sphere}/q_{cyl}, which was close to unity for size-independent *L/d* ratios, values of approx 1.15 are found for $d_{sphere} < 100\ \mu m$, while for particles with $d_{sphere} \sim 200\ \mu m$, an average value of 1–1.03 is found. The relatively large fraction of larger particles causes the tendency to values closer to unity in Fig. 11, where only averages over *L/d* were used to group the data. For the ratio q_{sphere}/q_{ell}, which has already shown larger deviations from unity for *L/d*-grouped data, these tendencies are repeated, with $q_{sphere}/q_{ell} < 0.9$ for $d_{sphere} < 100\ \mu m$ and $q_{sphere}/q_{ell} < 0.84$ for $d_{sphere} \sim 200\ \mu m$. For both burning rate ratios presented, the standard deviations are much smaller than the difference to unity, so that the effect based on the measurements is clearly proven.

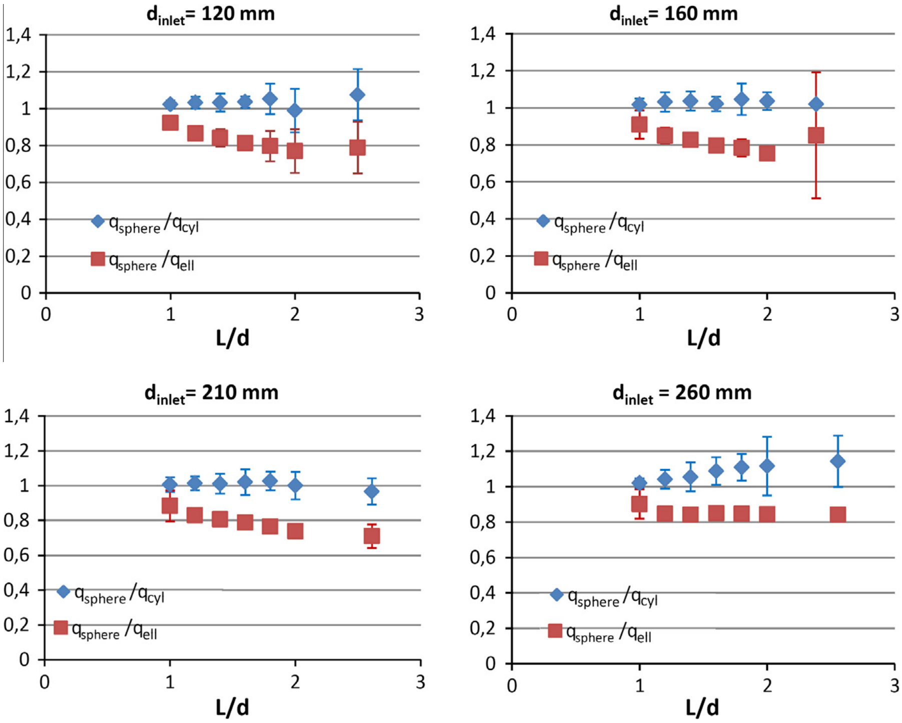

Fig. 11. Ratios of burning rates determined under assumption of cylindrical and elliptical particles, each compared to the burning rate of spherical particles.

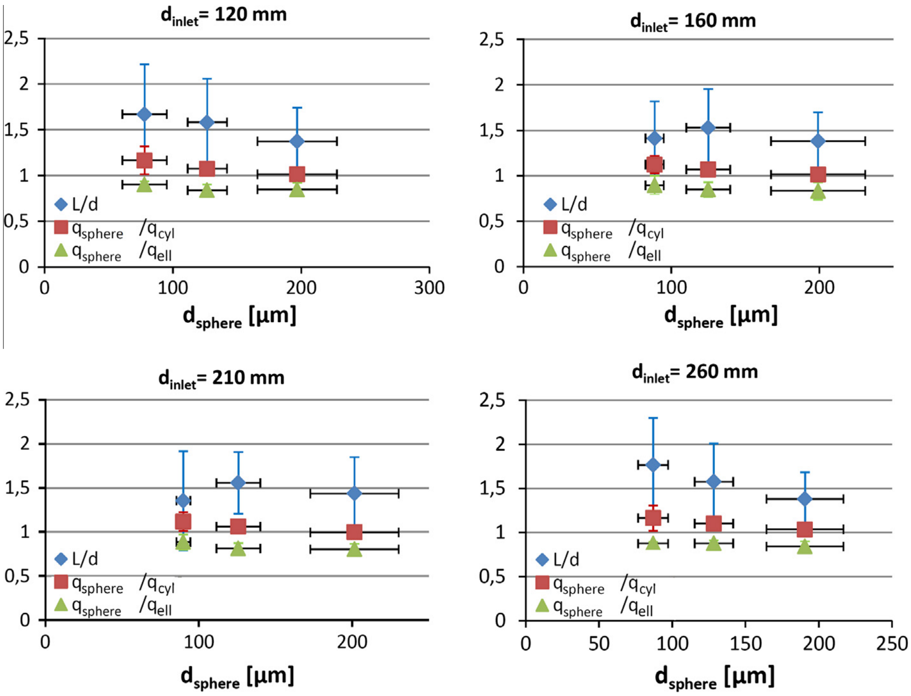

Fig. 12. *L/d* ratios and burning rate ratios for different d_{sphere}.

The larger effect of the particle shape on the burning rate determined for small particles points out the necessity to carefully analyse the particle shape simultaneously with temperature and particle size. This becomes even more important, as it is well known, that smaller particles are preferred for the determination of chemical rate parameters, as small particles are less affected by transport limitations. Furthermore, two-dimensional ratio pyrometry only measures a projection of the particle shape on the image plane, which underestimates the real (3d) L/d ratio, therefore the effect would become even larger when a stereoscopic technique could be applied under similar conditions.

From the results presented several questions arise which are out of the scope of the current work but should be discussed here briefly.

First, the current paper did present char burning rates. However, for the final use in CFD codes the char burning rates have to be converted to kinetic parameters typically modelled by an Arrhenius approach. The simplest assumption, frequently used in literature, for (oxidation only) kinetics is a single one-step Arrhenius expression:

$$q = A_o p_{O_2,s}^{n} e^{\left(-\frac{E_a}{RT_p}\right)}. \tag{9}$$

Typically, the pre-exponential factor A_o, the activation energy E_a and the reaction order n are calculated from burning rate measurements. Ways to derive the parameters for spherical particles are described by [9,11]. When we simplifying assume n and $p_{O_2,s}$ as being constant (n typically ranges from 0.5 to 1 according to classical Thiele analysis) Eq. (9) shows that an underestimation of q (ellipsoid particles) would lead to an underestimation of A_o, and overestimation of E_a. In addition it is clear from Eq. (9) that $p_{O_2,s}$ is needed to calculate A_o and E_a (and n). Note that the equation to calculate $p_{O_2,s}$ is itself diameter (i.e. shape) dependent [9,11]. Therefore, the final derivation of kinetic parameters needs further evaluation.

Second, as the burning rates calculated for cylindrical and ellipsoidal particles deviate from those of spherical particles in opposite directions, the question is which shape should be used for a specific fuel, or if one of the shapes is valid for all fuels. Coal particles which show even before combustion shapes similar to spheres and swelling during pyrolysis usually leads to further rounded particle shapes one could suggest an elliptical shape approximation because the lower limit of the elliptical shape is a sphere. For biomass fibres, the cylindrical shape appears to be promising. However, to answer the question of the “best” particle shape approximation, a more intense screening of different fuels with a wide-spread of experimental parameters (particle sizes, varying L/d ratios, and gas conditions) has to be carried out. Solid sampling at different stages of burn-out will be needed with subsequent microscopic analysis for further clarification.

Third, the question arises whether the error made by assuming sphericity for non-spherical particles is significant compared to the other uncertainties implied by the evaluation procedure for the char burning rate and subsequent kinetic parameters. The calculation of char burning rates is typically based a single-film boundary layer model [35]. The input parameters which are needed to solve the energy balance of the single film model, e.g. gas phase values like thermal conductivity, heat capacity, etc., particle properties like emissivity and char density, underlie certain uncertainties as well as measured values (temperature, particle shape). As the single film model, already including these uncertainties, has been investigated concerning its reliability to predict char consumption rates under pf-conditions for spherical particles [36,37] and did show good results compared to a detailed kinetic model, the error caused by particle shape negotiations (up to 18%) appears not negligible. In addition, the effect of Stefan flow, although small under the given conditions based on the results presented in [29], has to be added to the model, but is not supposed to exceed the difference caused by particle shape effects from the current point of view.

4. Conclusions

The typical energy balance equation, which has been used frequently to determine the burning rate and thus chemical rate parameters for char burning kinetics, has been adapted to cylindrical and prolate ellipsoidal particle shapes. Theoretical calculations have shown that the effect of particle shape variations cannot be neglected when pyrometric techniques are used to characterize the combustion of pulverized biomass. Also, experimental data were analysed to determine the influence of particle shape effects on the burning rates of a typical torrefied wood sample. The results point out the following findings:

- As the surface reaction rate of carbon $q = \dot{q}_{react}/\Delta H$ linearly depends on $\dot{q}_{react}$, it has to be expected that neglecting the particle shape leads to a miss-interpretation of the char burning rate for non-spherical particles.
- Regardless of the technique used to determine the burning rate of char particles, particle shape effects should be included in measurements used and models applied to determine kinetics parameters for further calculations.
- Both theoretical and experimental results show, that the two particle shapes considered have opposite effects on the calculated burning rate, especially for the typical particle shapes. The present work points out the necessity to identify which particle shapes considered is most consistent with burn out measurements from solid samples, which then enables to use the optical technique to characterize the shape depending burning behaviour of specific fuels.
- A very predictive technique to measure the particle shape simultaneously with the particle temperature could be stereoscopic (3d) imaging pyrometry. As the results from 2d-measurements show, it is possible to measure particle shape and temperature simultaneously, which leads to the possibility to include the geometric variability and its temporal alteration in models to describe char burning kinetics.
- Currently, commercial CFD-codes, which are used for predictive engineering of pf-boilers, do not include the particle shape in respect to the predicted burning rate. An inclusion of shape-corrected burning rate predictions for CFD-calculations should be developed and demonstrated.

Acknowledgment

This work has been financed by the German Research Foundation (DFG) within the project SCHI 1272/1-1.

References

[1] van Loo S, Koppejan J. Handbook of biomass combustion. London: Earthscan; 2008.

[2] Di Blasi C. Combustion and gasification rates of lignocellulosic chars. Prog Energy Combust Sci 2009;35:121–40.

[3] Senneca O, Cortese L. Kinetics of coal oxy-combustion by means of different experimental techniques. Fuel 2012;102:751–9.

[4] Fisher EM, Dupont C, Darvell LI, Commandré J-M, Saddawi A, Jones JM, et al. Combustion and gasification characteristics of chars from raw and torrefied biomass. Bioresour Technol 2012;119:157–65.

[5] Scheffknecht G, Al-Makhadmeh L, Schnell U, Maier J. Oxy-fuel coal combustion—a review of the current state-of-the-art. Int J Greenhouse Gas Control 2011;5:S16–35.

[6] Ballantyne TR, Ashman PJ, Mullinger PJ. A new method for determining the conversion of low-ash coals using synthetic ash as a tracer. Fuel 2005;84:1980–5.

[7] Mitchell R. On the temperature and reaction rate of burning pulverized fuels. Symp Combust 1982;19:1113–22.

[8] Tichenor DA, Mitchell RE, Hencken KR, Niksa S. Simultaneous in situ measurement of the size, temperature and velocity of particles in a combustion environment. Symp Combust 1985;20:1213–21.

[9] Mitchell R. experimentally determined overall burning rates of coal chars. Combust Sci Technol 1987;53:165–86.

[10] Hurt RH, Mitchell R. Unified high-temperature char combustion kinetics for a suite of coals of various rank. Symp Combust 1992;24:1243–50.

[11] Murphy J, Shaddix C. Combustion kinetics of coal chars in oxygen-enriched environments. Combust Flame 2006;144:710–29.

[12] Geier M, Shaddix CR, Davis K, Shim H-S. On the use of single-film models to describe the oxy-fuel combustion of pulverized coal char. Appl Energy 2012;93:675–9.

[13] Wornat M. Single-particle combustion of two biomass chars. Symp Combust 1996;26:3075–83.

[14] Cope RF, Monson CR, Germane GJ, Hecker WC. Improved diameter, velocity, and temperature measurements for char particles in drop-tube reactors. Energy Fuels 1994;8:925–31.

[15] Spliethoff H, Bauer C, Reichelt T, Hein KRG. Untersuchungen zum Abbrandverhalten und zur Alkalienfreisetzung an einem Druckflugstromreaktor. Erstes Statusseminar "Druckflamm", Ess.; 1999. p. 100–13.

[16] Joutsenoja T, Stenberg J, Hernberg R, Aho M. Pyrometric measurement of the temperature and size of individual combusting fuel particles. Appl Opt 1997;36:1525–35.

[17] Joutsenoja T, Saastamoinen J, Aho M, Hernberg R. Effects of pressure and oxygen concentration on the combustion of different coals. Energy Fuels 1999;13:130–45.

[18] Levendis YA, Estrada KR, Hottel HC. Development of multicolor pyrometers to monitor the transient response of burning carbonaceous particles. AIP; 2009.

[19] Levendis YA, Atal A, Courtemanche B, Carlson JB. Burning characteristics and gaseous/solid emissions of blends of pulverized coal with waste tire-derived fuel. Combust Sci Technol 1998;131:147–85.

[20] Bejarano PA, Levendis YA. Combustion of coal chars in oxygen-enriched atmospheres. Combust Sci Technol 2007;179:1569–87.

[21] Maffei T, Khatami R, Pierucci S, Faravelli T, Ranzi E, Levendis YA. Experimental and modeling study of single coal particle combustion in O_2/N_2 and Oxy-fuel (O_2/CO_2) atmospheres. Combust Flame 2013;160:2559–72.

[22] Hackert G, Wirtz S, Kremer H. Size, shape, velocity and temperature measurement of burning coal particles with a newly designed optical measurement technique – TOSCA. In: 9th Int symp appl laser tech to fluid mech; 1998.

[23] Schiemann M, Scherer V, Wirtz S. Optical coal particle temperature measurement under oxy-fuel conditions: measurement methodology and initial results. Chem Eng Technol 2009;32:2000–4.

[24] Sampath R, Maloney DJ, Zondlo JW, Woodruff SD, Yeboah YD. Measurements of coal particle shape, mass, and temperature histories: Impact of particle irregularity on temperature predictions and measurements. Symp Combust 1996;26:3179–88.

[25] Lu H, Ip E, Scott J, Foster P, Vickers M, Baxter LL. Effects of particle shape and size on devolatilization of biomass particle. Fuel 2010;89:1156–68.

[26] Arias B, Pevida C, Fermoso J, Plaza M, Rubiera F, Pis J. Influence of torrefaction on the grindability and reactivity of woody biomass. Fuel Process Technol 2008;89:169–75.

[27] Ciolkosz D, Wallace R. A review of torrefaction for bioenergy feedstock production. Biofuels Bioprod Biorefin 2011;5:317–29.

[28] Field MA, Gill DW, Morgan BB, Hawksley PGW. Combustion of pulverized coal. Leatherhead (England): The British Coal Utilization Research Association; 1967.

[29] Murphy J, Shaddix C. Effects of Stefan flow on heat transfer from reacting carbon particles. Sandia-Report 2003–8720J; 2003.

[30] Kalinchak VV, Orlovskaya S, Prudnikova YV. Effect of Stefan flow on combustion characteristics of a moving carbon particle. Combust Explos Shock Waves 2001;37:402–5.

[31] Wadewitz A, Specht E. Limit value of the Nusselt number for particles of different shape. Int J Heat Mass Trans 2001;44:967–75.

[32] Khatami R, Stivers C, Levendis YA. Ignition characteristics of single coal particles from three different ranks in O_2/N_2 and O_2/CO_2 atmospheres. Combust Flame 2012;159:3554–68.

[33] Chen L, Dupont C, Salvador S, Grateau M, Boissonnet G, Schweich D. Experimental study on fast pyrolysis of free-falling millimetric biomass particles between 800 °C and 1000 °C. Fuel 2013;106:61–6.

[34] Paul PH. DRFM: a new package for the evaluation of gas-phase transport properties. Albuquerque, NM, and Livermore, CA (United States); 1997, http:\\dx.doi.org\10.2172/565553.

[35] Turns SR. An introduction to combustion: concepts and applications. 2nd ed. McGraw-Hill; 2000.

[36] Hecht ES, Shaddix CR, Lighty JS. Analysis of the errors associated with typical pulverized coal char combustion modeling assumptions for oxy-fuel combustion. Combust Flame 2013;160:1499–509.

[37] Gonzalo-Tirado C, Jiménez S, Johansson R, Ballester J. Comparative study of four alternative models for CO oxidation around a burning coal char particle. Combust Flame 2014;161:1085–95.